OPEN ACCESS



Global MHD Simulations of the Time-dependent Corona

Roberto Lionello ®, Cooper Downs ®, Emily I. Mason ®, Jon A. Linker ®, Ronald M. Caplan ®, Pete Riley ®, Viacheslav S. Titov ®, and Marc L. DeRosa ® Predictive Science Inc., 9990 Mesa Rim Rd., Ste. 170, San Diego, CA 92121, USA; lionel@predsci.com Lockheed Martin Solar and Astrophysics Laboratory, 3251 Hanover Street B/203, Palo Alto, CA 94304, USA

Received 2023 July 20; revised 2023 September 28; accepted 2023 October 2; published 2023 December 8

Abstract

We describe, test, and apply a technique to incorporate full-Sun, surface flux evolution into an MHD model of the global solar corona. Requiring only maps of the evolving surface flux, our method is similar to that of Lionello et al., but we introduce two ways to correct the electric field at the lower boundary to mitigate spurious currents. We verify the accuracy of our procedures by comparing to a reference simulation, driven with known flows and electric fields. We then present a thermodynamic MHD calculation lasting one solar rotation driven by maps from the magnetic flux evolution model of Schrijver & DeRosa. The dynamic, time-dependent nature of the model corona is illustrated by examining the evolution of the open flux boundaries and forward-modeled EUV emission, which evolve in response to surface flows and the emergence and cancellation flux. Although our main goal is to present the method, we briefly investigate the relevance of this evolution to properties of the slow solar wind, examining the mapping of dipped field lines to the topological signatures of the "S-Web" and comparing charge state ratios computed in the time-dependently driven run to a steady-state equivalent. Interestingly, we find that driving on its own does not significantly improve the charge state ratios, at least in this modest resolution run that injects minimal helicity. Still, many aspects of the time-dependently driven model cannot be captured with traditional steady-state methods, and such a technique may be particularly relevant for the next generation of solar wind and coronal mass ejection models.

Unified Astronomy Thesaurus concepts: Magnetohydrodynamical simulations (1966); Solar corona (1483) Supporting material: animations

1. Introduction

Surface magnetic fields are the key observational input to coronal and solar wind models. Used as the inner boundary condition, it is the distribution, polarity, and strength of the radial magnetic field, B_r , at the surface that defines the ground state of the corona (the potential field) and largely determines the topology and geometric features of the corona's magnetic field at global scales (coronal holes and streamers). It is also the evolution of the surface flux, which includes the shearing, emergence, and cancellation of magnetic features, that determines how energy is stored and released in the corona. As such, ground- and space-based observatories routinely measure photospheric and chromospheric magnetic observables, which are then used to create coronal models.

With the exception of the PHI instrument on board the Solar Orbiter spacecraft (Solanki et al. 2020), current ground- and space-based observatories provide only an Earth-centered view of the photospheric magnetic flux on the Sun. The average rotation period of the Sun as viewed from Earth, known as a Carrington rotation (CR), is \approx 27.3 days, so a traditional approach for constructing model boundary conditions has been to use full-Sun Carrington synoptic maps. These maps are built up by combining the data near central meridian from full-disk magnetograms as the Sun rotates. As such, changes in the average shape and structure of the corona in time have often been characterized in a variety of models on CR-to-CR basis,

Original content from this work may be used under the terms of the Creative Commons Attribution 4.0 licence. Any further distribution of this work must maintain attribution to the author(s) and the title of the work, journal citation and DOI.

ranging from simple potential field source surface (PFSS) extrapolations to full magnetohydrodynamic (MHD) calculations. In this modeling paradigm, successive monthly "snapshots" of the corona are computed separately, with each calculation for a given CR being fully independent of the previous case (e.g., Riley et al. 2006; Luhmann et al. 2022).

On the other hand, we know full well that many of the most intriguing and important phenomena in the corona (solar flares, jet eruptions, coronal mass ejections (CMEs), etc.) are inherently driven by surface flux evolution at timescales from minutes to days depending on the spatial scale of interest (Webb & Howard 2012; Raouafi et al. 2016; Benz 2017, and references therein). Similarly, at the largest temporal and spatial scales (i.e., global scales) surface flux evolution is responsible for the formation and evolution of helmet streamers and pseudostreamers over days to months, which is thought to play an important role in the processing of solar wind and ejecta as smaller structures erupt or migrate across their boundaries (Higginson et al. 2017; Scott et al. 2021; Wyper et al. 2021). How these large-scale closed structures evolve in response to surface changes and subsequently reconnect through interchange reconnection with nearby open fields has important implications for our understanding of switchbacks measured by the Parker Solar Probe (Fisk & Kasper 2020; Zank et al. 2020; Telloni et al. 2022), as well as the formation of composition and charge-state variations in the solar wind (Zurbuchen et al. 2002; Kepko et al. 2016).

In the context of global coronal models, one way to incorporate time evolution at the inner boundary is by leveraging the outputs of surface flux transport (SFT) models. SFT models describe the time evolution of magnetic flux over

the full sphere by incorporating various evolutionary processes: typically differential rotation, meridional flow, supergranular diffusion, and random flux emergence. Such models can also assimilate magnetograms from available observatories to produce a continuous approximation of the state of the photospheric magnetic field, also known as a sequence of synchronic maps. Using this approach, SFT models have been successful in predicting the evolution of photospheric magnetic fields (Wang et al. 1991; Worden & Harvey 2000; Schrijver & DeRosa 2003; Arge et al. 2010; Upton & Hathaway 2014).

The magnetic flux information from an SFT model can subsequently be processed to create the full-Sun boundary condition of B_r for the global coronal magnetic field model. With a time sequence of synchronic maps, it then becomes possible to model successive states of the corona and heliosphere at a much smaller time interval than one CR. This can be done by running successive (but independent) 3D calculations at the cadence of the synchronic maps (e.g., Odstrcil et al. 2020), or by driving the model at the inner boundary using electric fields derived from the evolving sequence of B_r (e.g., Weinzierl et al. 2016). The latter, "driven" approach is physically more attractive, as it allows one to capture how surface flux evolution imprints a dynamical "memory" in the system as it evolves from state to state, and it allows for the build up of magnetic stresses and energy in time at the correct dynamical timescales.

On the other hand, deriving an appropriate driving electric field from a sequence of B_r maps is both challenging and not fully constrained (Fisher et al. 2010; Cheung & DeRosa 2012; Yeates 2017; Lumme et al. 2017). For global coronal field models, such driving was studied with the simplified magnetofrictional approach by Weinzierl et al. (2016), who focused on the importance of the noninductive freedom in the boundary electric field. While convenient for studying energy injection and storage, magnetofrictional models fundamentally cannot capture the dynamical timescales of the system (set by the magnetoacoustic speeds), non-force-free processes (such as eruptions), or how the 3D plasma state of the corona and solar wind evolve in tandem with surface flux changes (flows, density, temperature). Another challenge for full-Sun, global driving is the fact that data assimilation in SFT models, which ingests new measurements from the Earth-Sun line as the Sun rotates, will instantaneously overwrite existing flux. These imposed changes imprint both an unphysical dynamical timescale and forcing on the system, as well as a floating magnetic monopole that must (typically) be corrected by some means.

In this light, we describe our efforts to develop and test a suitable boundary driving approach for global MHD models of the solar corona. In Section 2, using a technique similar to that of Lionello et al. (2013), we illustrate how a full electric field may be expressly determined from time-evolving B_r maps and the flow profile from an SFT model. At the boundary, the electric field obtained through our formulation evolves the magnetic field smoothly at the code time step, thus avoiding the instantaneous overwriting of the flux. We also discuss additional corrections that can help eliminate spurious currents at the inner boundary of the MHD model. In Section 3 we test and compare the various approaches on an idealized case where the true surface flows are known.

Next, in Section 4 we demonstrate the approach in a full thermodynamic MHD calculation for 1 month of coronal

evolution, which is driven by a sequence of magnetic flux maps provided by the Lockheed Evolving Surface-Flux Assimilation Model (ESFAM; Schrijver & DeRosa 2003). This particular ESFAM run does not assimilate data but is instead designed to vield Sun-like evolution with an average strength sunspot cycle at solar minimum conditions. This provides a smoothly evolving full-Sun SFT data set without the typical artifacts of data assimilation. To characterize the results, we calculate EUV synthetic emission images, as well as maps of coronal hole locations, the squashing factor (O; Titov 2007), dips in magnetic field lines, and fractional charge states. To evaluate the importance of time-dependent evolution, we also compare these results with those of steady-state models. Finally, we conclude in Section 5 by discussing our results in the context of the solar wind, as well as the relevance of these techniques for future applications.

2. Parameterizing Full-Sun Boundary Evolution In MHD

2.1. The MAS MHD Model

To develop, test, and study methods for evolving the magnetic flux at the inner boundary of an MHD model, we employ the Magnetohydrodynamic Algorithm outside a Sphere (MAS) code. MAS is designed to model the global solar atmosphere from the top of the chromosphere to Earth and beyond and has been used extensively to study coronal structure (Mikić et al. 1999, 2018; Linker et al. 1999; Lionello et al. 2009; Downs et al. 2013), coronal dynamics (Lionello et al. 2005, 2006; Linker et al. 2011), and CMEs (Linker et al. 2003; Lionello et al. 2013; Török et al. 2018). MAS solves the resistive, thermodynamic MHD equations in spherical coordinates (r, θ, ϕ) on structured nonuniform meshes. Magnetosonic waves are treated semi-implicitly, allowing us to use large time steps for the efficient computation of long-time evolution. The semi-implicit method is not harmful for obtaining timedependent solutions, as it introduces dispersive effects only for processes occurring on timescales shorter than or equal to the time step (Schnack et al. 1987). Given that the flows that drive evolution of flux at the surface are much smaller than the typical coronal flow speeds that set the CFL limit and time step in the model, the semi-implicit method is more than suitable for the time-dependently driven calculations described here.

The present version of MAS allows for several modes of operation that govern which terms are solved for and/or added to the MHD equations. Here we use the term "thermodynamic MHD" to indicate that MAS solves for additional transport terms that describe energy and momentum flow in the solar corona and solar wind (coronal heating, parallel thermal conduction, radiative loss, and Alfvén wave acceleration; as fully described in Appendix A of Török et al. 2018).

The latest version of the thermodynamic mode in MAS also includes a physics-based specification of the coronal heating term through a wave-turbulence-driven (WTD) phenomenology. In this approach, additional equations are solved to capture the macroscopic propagation, reflection, and dissipation of low-frequency Alfvénic turbulence. The physical motivation underlying the WTD approach is that outward and reflecting Alfvén waves interact with one another, resulting in their dissipation and heating of the corona (e.g., Zank et al. 1996; Verdini & Velli 2007). This follows related works, where the general formalism for the propagation of Alfvén waves (e.g., Heinemann & Olbert 1980; Zank et al.

1996, 2012) is usually approximated to produce tractable equations for the propagation of the energy density or the amplitude of the Alfvén waves (e.g., Velli 1993; Matthaeus et al. 1999; Dmitruk et al. 2001; Cranmer et al. 2007; Verdini & Velli 2007; Breech et al. 2008; Chandran & Hollweg 2009; Usmanov et al. 2011; Jin et al. 2012; Sokolov et al. 2013; van der Holst et al. 2014; Oran et al. 2015). A full description of the MAS-WTD model and equations solved is provided in the supplementary materials of Mikić et al. (2018).

We have also recently incorporated into MAS a none-quilibrium ionization module to advance the fractional charge states of minor ions according to the model of Shen et al. (2015):

$$\frac{\partial_{Z}F^{i}}{\partial t} + \mathbf{v} \cdot \nabla_{Z}F^{i} = n_{e}[{}_{Z}C^{i-1}{}_{Z}F^{i-1} - ({}_{Z}C^{i} + {}_{Z}R^{i-1}){}_{Z}F^{i} + {}_{Z}R^{i}{}_{Z}F^{i+1}].$$
(1)

For an element with atomic number Z, ${}_{Z}F^{i}(r, \theta, \phi)$ indicates the fraction of ion i+(i=0, Z) with respect to the total at a grid point:

$$\sum_{i=0}^{Z} {}_{Z}F^{i} = 1. {2}$$

For each element, the ion fractions are coupled through the ionization, ${}_{Z}C^{i}(T)$, and recombination, ${}_{Z}R^{i}(T)$, rate coefficients derived from the CHIANTI atomic database (Dere et al. 1997; Landi et al. 2013). Here T, n_{e} , and v are the temperature, number density, and velocity of the plasma, respectively. This module has been tested in our hydrodynamic 1D, WTD wind code (Lionello et al. 2019). A similar time-dependent 3D model of charges states of minor ions is shown in Szente et al. (2022).

2.2. Incorporating Magnetic Flux Maps

To drive the magnetic field evolution in MAS, we can evolve the radial component of the magnetic field at the boundary using a technique similar to that described by Lionello et al. (2013). We specify the tangential electric field at the boundary $E_{10}(\theta, \phi, t)$ as

$$\mathbf{E}_{t0} = \nabla_{t} \times \Psi \hat{\mathbf{r}} + \nabla_{t} \Phi. \tag{3}$$

The potential Ψ controls the evolution of the normal component of the magnetic field B_{r0} ,

$$\nabla_t^2 \Psi = \frac{\partial B_r}{\partial t}.\tag{4}$$

We use a sequence of full-Sun $B_r(\theta, \phi)$ maps in time to specify the evolution of Ψ using Equation (4). Since the temporal cadence of the input maps will generally be much slower than the MHD model time step, we must interpolate B_r in time at every step. Because linear interpolation of the B_r maps in time implies a discontinuous $\partial B_r/\partial t$ as we shift from the interval between one pair of maps to the next, one must use a higher-order interpolation scheme to ensure a smooth step-to-step evolution of the electric field at the inner boundary. Here we use a simple piecewise cubic Hermite interpolation scheme (Fritsch & Carlson 1980), to ensure continuity in at least the first derivative and to preserve monotonicity in the evolution of $B_r(t)$ at all points within the time interval between maps.

Next, the potential $\Phi(\theta, \phi, t)$ can be completely specified if the flows that led to the evolution are known, i.e., we can find Φ from the equation

$$\nabla_t^2 \Phi = -\nabla_t \cdot (\boldsymbol{v} \times \boldsymbol{B})_t. \tag{5}$$

In general, however, the full-Sun distributions of the complete flow and magnetic field vectors responsible for map-to-map B_r changes are not typically available from observations or SFT models that assimilate observational data. Instead, we can incorporate the known large-scale flows (differential rotation and meridional flows) to at least include their contribution to the transverse electric field. In other words, while the Φ potential solve ensures that we can evolve flux to exactly match the B_r component of the maps, the magnetic fields that evolve and emerge will generally have less shear and twist than is observed (especially for active regions). On the other hand, this method has a significant advantage over more complex or localized techniques in that vector magnetic field observables and/or flow correlation tracking are not required. Furthermore, additional energization can easily be explored through the freedom in the Φ potential³, which will be explored in future work.

At this point the Ψ and Φ potentials only provide information about the transverse electric field. Our next aim is to find a full boundary electric field, E_0 , that (1) is minimally diffusive and (2) causes minimal boundary layers. A possible solution is to prescribe the condition of ideal MHD at the lower boundary (method A):

$$\boldsymbol{E}_0 \cdot \boldsymbol{B}_0 = E_r B_r + \boldsymbol{E}_{t0} \cdot \boldsymbol{B}_{t0} = 0, \tag{6}$$

where t means the component tangential to the boundary of the B_0 and E_0 fields. From that it follows that

$$E_r = -\frac{\boldsymbol{E}_{t0} \cdot \boldsymbol{B}_{t0}}{\boldsymbol{B}_r},\tag{7}$$

which can be regularized using a small parameter ϵ as

$$E_r^* = -\frac{(\boldsymbol{E}_{t0} \cdot \boldsymbol{B}_{t0})B_r}{B_r^2 + \epsilon^2}.$$
 (8)

This method has the disadvantage of introducing artificial reconnection at the polarity inversion line (PIL), where $B_r = 0$.

Building on method $\tilde{\mathbf{A}}$, we can compute an additional correction to the boundary electric field, $\tilde{\mathbf{E}}_0$, such that $\tilde{\mathbf{E}}_0 \cdot \mathbf{B}_0 \simeq 0$ everywhere by slightly modifying \mathbf{E}_{t0} and E_r^* near the neutral line (method B). To define $\tilde{\mathbf{E}}_0$, we use

$$\mathbf{v}_{\perp}^* = \frac{\mathbf{E}_0 \times \mathbf{B}_0}{\mathbf{B}^2},\tag{9}$$

which is the flow associated with E_0 as calculated with A,

$$\tilde{\boldsymbol{E}}_0 = -\boldsymbol{v}_{\perp}^* \times \boldsymbol{B}_0. \tag{10}$$

We obtain

$$\tilde{E}_{r_0} = \left(1 + \frac{\epsilon^2}{B^2}\right) \frac{E_{t_0} \cdot B_{t_0}}{B_{r_0}^2 + \epsilon^2} B_{r_0},\tag{11}$$

³ See the MAS energization examples in Yeates et al. (2018) and Mikić et al. (2018), where a full-Sun Φ potential is specified in a semiautomated procedure to emerge a sheared magnetic field along arbitrary neutral lines.

$$\tilde{E}_{t_0} = E_{t_0} - \frac{\epsilon^2 E_{t_0} \cdot B_{t_0}}{B_0^2 (B_{t_0}^2 + \epsilon^2)} B_{t_0}.$$
 (12)

Whether method A or B is used, we derive again the boundary flow, \tilde{v}_0 , using the boundary electric field expression provided by either method,

$$\tilde{\mathbf{v}}_0 = \frac{\tilde{\mathbf{E}}_0 \times \mathbf{B}_0}{\epsilon^2 + B_0^2},\tag{13}$$

where we add a small parameter ϵ to regularize the flow at the neutral line.

Only for method B, we also add a small resistivity value at the boundary PIL:

$$\tilde{\eta} \propto \left| \frac{\partial \sin \theta \tilde{E}_{\phi}}{\partial \theta} - \frac{1}{\sin \theta} \frac{\partial \tilde{E}_{\theta}}{\partial \phi} - \left(\frac{\partial \sin \theta E_{\phi}}{\partial \theta} - \frac{1}{\sin \theta} \frac{\partial E_{\theta}}{\partial \phi} \right) \right|, \tag{14}$$

where we dropped the subscript 0 from the notation.

2.3. Asymptotic Values at the PIL

Because each method requires some form of regularization near the PIL, it follows that we should seek a robust dimensionless formulation that is equally appropriate for all types of broad/compact and weak/strong flux distributions on the Sun.

We can rewrite Equation (8) in terms of $f = \epsilon^2/B_r^2$ and obtain

$$\frac{|E_r^0|}{|E_{t0}|} \propto \frac{|B_{t0}|}{|B_r|(1+f)}.$$
 (15)

The right-hand side (rhs) of Equation (15) can be easily computed at any state of the simulation, regardless of dB_r/dt or the full electric field itself. We seek a definition of f such that E_r is bounded near the PIL and f is controlled by a dimensionless constant, unlike ϵ , which is in units of B. Let us therefore find a form of f so that the rhs of Equation (15) will reach a fixed, asymptotic value when $B_0 \rightarrow 0$. We simply define f as

$$f = A \frac{|\mathbf{B}_T|}{|B_r|},\tag{16}$$

where A is a dimensionless constant and 1/A sets the largest value for the left-hand side of Equation (15). The new form assumed by Equation (8) is thus the following:

$$E_r^* = -\frac{E_{t0} \cdot B_{t0} \operatorname{sign}(B_r)}{|B_r| + A|B_{t0}|}.$$
 (17)

Similarly, we seek a new formulation for the boundary flow \tilde{v}_0 in Equation (13) that will converge to a meaningful asymptotic value for \tilde{v}_0 , when $B_0 \rightarrow 0$ at the PIL. We rewrite Equation (13) as

$$\tilde{\mathbf{v}}_0 = \frac{\tilde{\mathbf{E}}_0 \times \mathbf{B}_0}{B_0^2 (1+g)},\tag{18}$$

where g is a dimensionless quantity. We proceed heuristically by comparing \tilde{v}_0 to the local sound speed, calculating the magnitude, and dividing by c_s to obtain

$$\frac{|\tilde{\mathbf{v}}_0|}{c_s} = \frac{|\tilde{\mathbf{E}}_0||\mathbf{B}_0|\sin\theta}{c_s B_0^2 (1+g)} = \frac{\tilde{\mathbf{E}}_0 \sin\theta}{c_s B_0 (1+g)}.$$
 (19)

Then, we pose

$$g = D \frac{\tilde{E}_0}{c_s B_0},\tag{20}$$

where D is a dimensionless constant, and insert this into Equation (19). The ratio simplifies as

$$\frac{\tilde{\mathbf{v}}_0}{c_s} = \frac{\tilde{E}_0 \sin \theta}{c_s B_0 + D\tilde{E}_0},\tag{21}$$

which converges to 1/D as $B_0 \rightarrow 0$. In other words, 1/D specifies the maximum fraction of $|\tilde{v}_0|$ relative to the local sound speed at the boundary. The new formulation of \tilde{v}_0 thus becomes

$$\tilde{\mathbf{v}}_0 = \frac{\tilde{\mathbf{E}}_0 \times \mathbf{B}_0}{B_0^2 + D\tilde{\mathbf{E}}_0 B_0 / c_s}.$$
 (22)

3. Test of the Corrections

To evaluate the performance of the correction methods in Section 2.2, we can apply them to a solution where the true electric field that evolved the boundary is known. To this end, we apply them to time-dependent simulations driven with the magnetic flux maps extracted from the 3D MHD coronal solution of Lionello et al. (2005, 2020). These employed the polytropic model of Linker et al. (1999) to study the effects of differential rotation on a photospheric magnetic field distribution similar to that of Wang et al. (1996). This consists of a global dipole distribution with a bipolar active region superimposed (see also Figure 2). After a relaxation period lasting until t = 150 code units (1 CU = 1445.87 s), they turned the following surface flow on:

$$\omega(\theta) = 13.39 - 2.77 \cos^2 \theta \, \deg \, \mathrm{day}^{-1},\tag{23}$$

which is 10 times the value of Wang et al. (1996). We repeated this run in the same manner, evolving the surface field directly using the prescribed $E = -v \times B$ from the driving flow (only v_{ϕ} in this case) and B_0 at a given time step. We label this run with O (original) and sample the values of B_r on the solar surface with a 1 CU cadence.

Then, we use the surface B_r maps from O to run four simulations using Equations (4)–(5) to prescribe the electric field at the $r=R_{\odot}$ surface: the first run is uncorrected (U; i.e., neither of the methods of Section 2.2 is applied, but the "true" radial electric field is used, $E_r^0=\omega R_{\odot}B_{\theta}^0$), the second run (E) is erroneously driven with $E_r^0=0$, the third run is corrected with method A, and the fourth is corrected with method B.

In Figure 1 we present the time histories of the four runs from the inception of photospheric flows at t=150 until t=170. Panels (a)–(f) show quantities integrated over the whole computational domain. With the exception of currents, the U run presents values coincident with those of the O run in all panels. The magnetic energies (Figure 1(a)) of the four runs are also practically indistinguishable. However, following the introduction of differential rotation at t=150, the kinetic energies (Figure 1(b)) of the A- and B-driven runs are $\sim 1\%$ smaller than the that of the reference O run. This behavior is replicated in the time history of the magnetic energy in Figure 1(c). The integrated Lorentz force (Figure 1(d)) shows a jump at t=150 for all runs, with the curve of the O and U runs bracketed by those of the corrected runs A and B. The last integrated quantity $|J \cdot B|$ measures the deviation from ideal

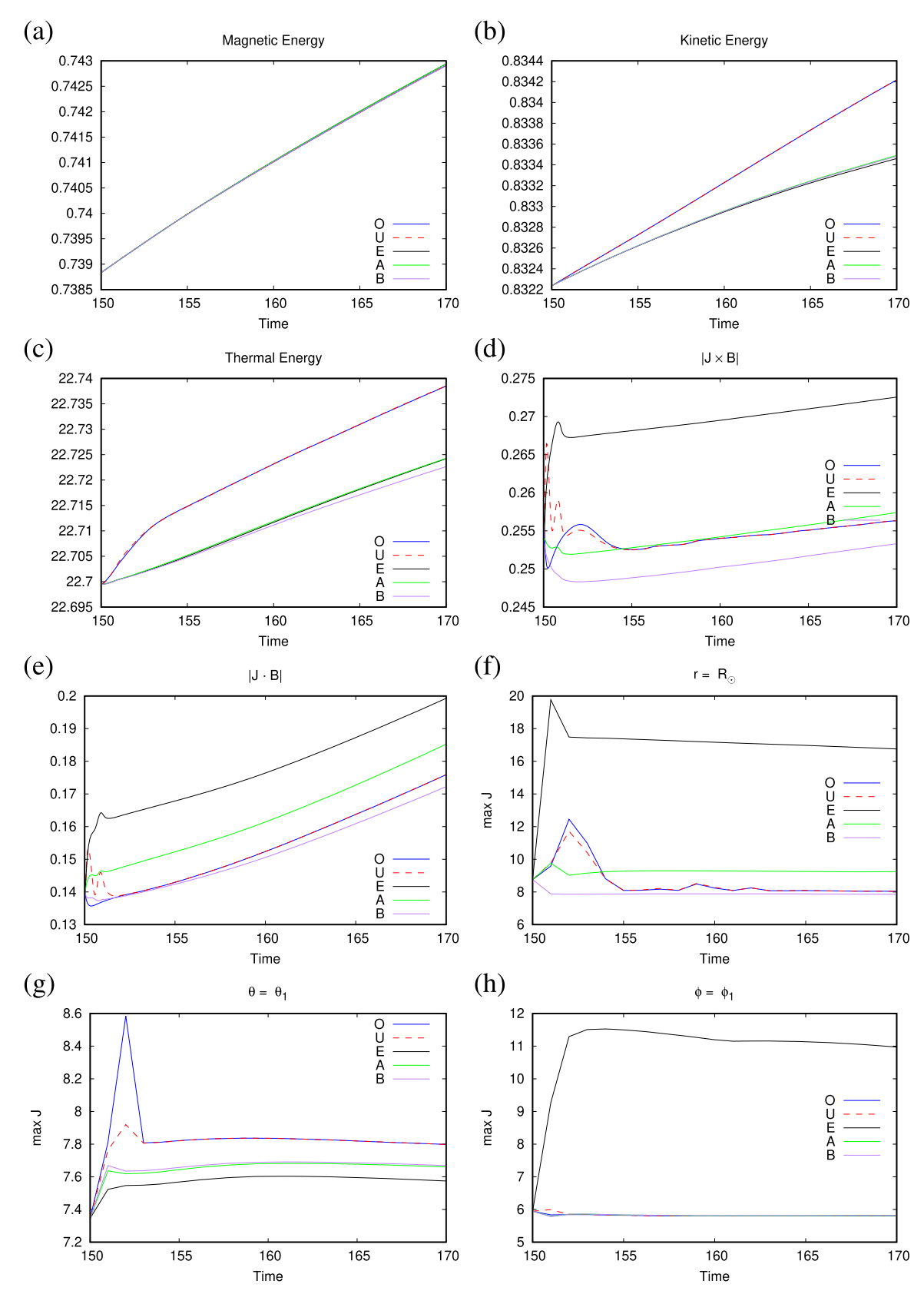


Figure 1. Time histories of the simulations respectively labeled 0, U, E, A, and B in Section 3. Shown are volume integrals of the magnetic energy (panel (a)), the kinetic energy (panel (b)), the thermal energy (panel (c)), $|J \times B|$ (panel (d)), and $|J \cdot B|$ (panel (e)). Maximum current density J is evaluated on the surfaces $r = R_{\odot}$ (panel (f)), $\theta = \theta_0$ (panel (g)), and $\phi = \phi_0$ (panel (h)). The locations of θ_0 and ϕ_0 are shown in the top left panel of Figure 2.

MHD. Similarly to panel (d), U and O are between A and B. The erroneous run, E, has larger values of the integrated Lorentz force and parallel current.

We also examine the history of the maximum current density J on three orthogonal cut planes in spherical coordinates: the $r=R_{\odot}$ surface encompasses the whole active region, the $\theta=\theta_0$

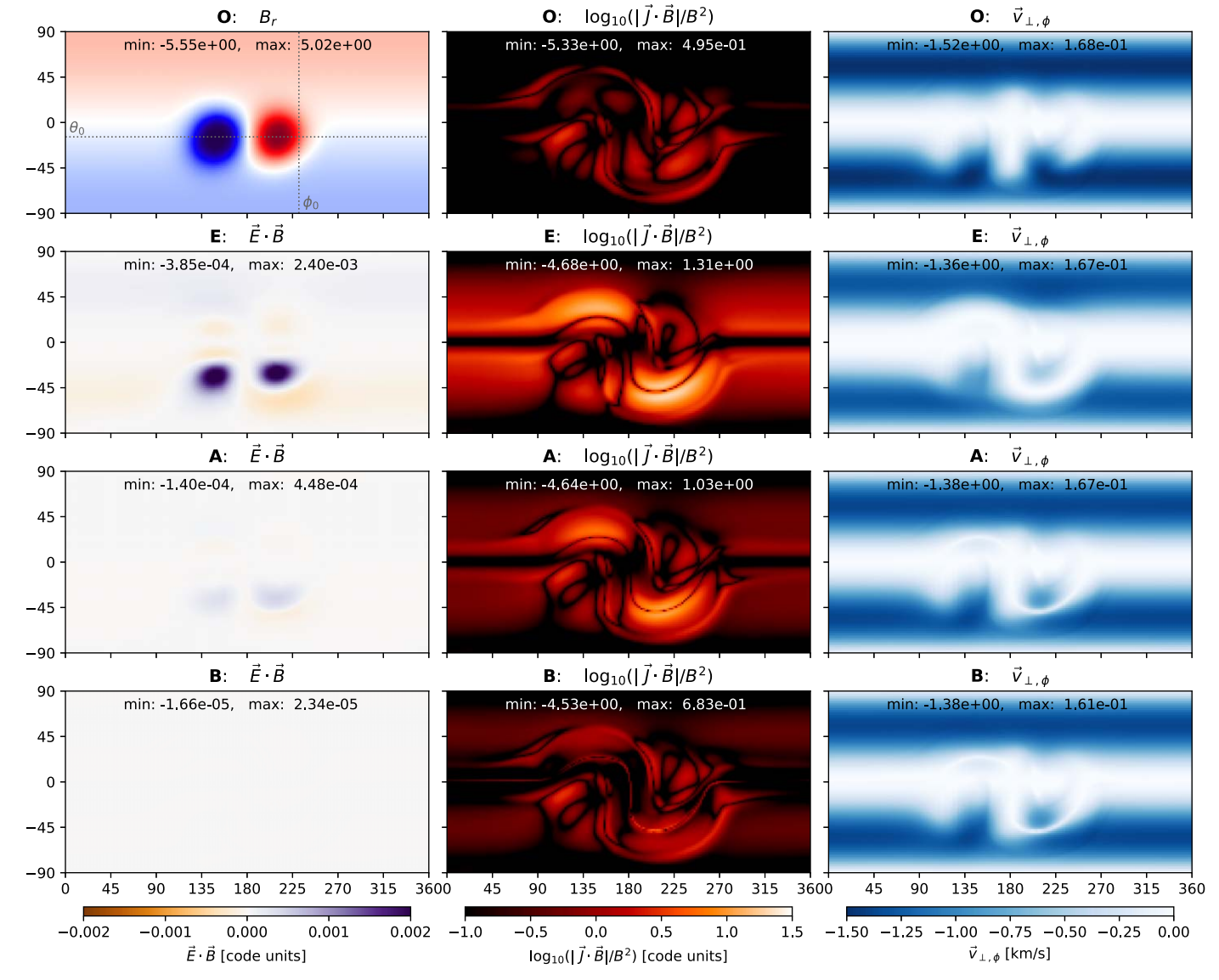


Figure 2. 2D maps of surface quantities at the final step (t = 170 CU) for test cases O, E, A, and B. The top left panel shows B_r at this time for reference, and the positions of the θ_0 and ϕ_0 cut planes used in Figure 1 are indicated with the dotted gray lines. The remaining panels in the left column show $E \cdot B$ for each case, where E is the driving electric field. The middle column shows $\log_{10}(|J \cdot B|/B^2)$ for all four runs. The right column shows the ϕ component of the driving velocity that is perpendicular to B ($v_{\perp,\phi}$). For each map, the minimum and maximum of the plotted quantity at the surface are shown.

surface intersects the active region, and the $\phi=\phi_0$ lies west of the positive polarity. When the flows are turned on at t=150, we notice in panel (f) a sudden spike on the $r=R_\odot$ surface for the O and U runs, while the enhancements for A and B are much smaller. As was the case for the global measurements in panels (d) and (e), the O and U values soon become bracketed by those of A and B. Run E shows high values of the maximum currents on the $r=R_\odot$ and $\phi=\phi_0$ surfaces. Panels (g) and (h) show that, with the exception of E, all the driven runs manage to reproduce the maximum J on $\theta=\theta_0$ and $\phi=\phi_0$ surfaces in substantial agreement with the O run.

To convey a more intuitive sense of how the corrections operate, we show full-Sun surface maps of various quantities at the final state of runs O, E, A, and B in Figure 2 (skipping U because it is essentially the same as O). First, to illustrate the shape and location of the PIL near the large bipolar region, the top left panel shows the full-Sun B_r distribution. The remaining panels in the left column show $E \cdot B$ for the computed electric

field for runs E, A, and B ($E \cdot B$ is zero for O by construction). As expected, $E \cdot B$ is largest when E_r is ignored altogether in run E, and the signature is strongest near the largest fields along the the PIL. Method A reduces the maximum $E \cdot B$ compared to run E by just over a factor of 5, while method B effectively eliminates it as intended.

The middle column of Figure 2 illustrates how field-aligned currents build up at the boundary in each case, showing a map of $\log_{10}(|\boldsymbol{J}\cdot\boldsymbol{B}|/B^2)$. Compared to the reference case O, all runs introduce some level of additional currents, but the features change from case to case. As expected, by not applying any $\boldsymbol{E}\cdot\boldsymbol{B}=0$ correction, run E builds up the largest boundary layer, especially near the main PIL of the two polarities. Method A attenuates this current signature by a factor of two or more (note the \log_{10} scaling of the min/max values), while method B attenuates this signal even further. However, right at the PIL for run B we see a slight enhancement of $\boldsymbol{J}\cdot\boldsymbol{B}$ compared to the other runs, which is the signature of the small

resistivity that is active where $B_r \rightarrow 0$ that is needed to ensure that the B_r evolution matches the driving sequence of maps (Equation (14)).

Lastly, the right panels of Figure 2 show maps of the longitudinal component of the velocity field perpendicular to Bat the inner boundary, $v_{\perp,\phi}$. For run O this is simply the component of the differential rotation flow that actually moves the field eastward, while for the remaining cases this component is determined from Equation (22). For E, A, and B we see that the true driving flow is largely recovered everywhere except near the PIL of the flux concentrations. Methods A and B do a better job than run E near the PIL, especially in filling in the strong patches of $v_{\perp,\phi}$ to the southeast and northwest of the central PIL segment. That said, on the opposite side of the Sun, where dipolar flux distribution is basically symmetric north-south (and thus B_r is not changing), the maximum strength of $|v_{\perp,\phi}|$ is not quite recovered. This stems from the fact that the PIL for the global dipole is very broad, such that the truncation function for determining E_r^0 (Equation (16)) is not quite zero even at midlatitudes.

In summary, these test runs illustrate the inherent limitations of recovering a suitable electric field to drive surface flux evolution from limited information (a sequence of full-Sun B_r maps in time), as well as the pros and cons of the various methods. When the full surface flow profile is known, the combination of E_t derived from the Ψ and Φ potential solves and the true E_r , which can be computed if the exact surface flow is known, reproduces the true solution (runs O vs. U). When E_r is not available, which will be generally true when only the full-Sun evolution of B_r and the average macroscopic flows are known (i.e., flux transport models assimilating observations), it must be computed from available information (runs A vs. B) or ignored (run E).

Although both correction methods A and B appear to give similar results, method B is able to completely eliminate the nonideal part of the electric field, which may help it perform better when strong magnetic flux is carefully emerged (e.g., during the simulations of CMEs). On the other hand, the advantages of method B come at the cost of an additional free parameter $(\tilde{\eta})$ and concentrating the resistive boundary layer right at the PIL. In favor of smoothness and simplicity, we thus opt to use method A in our first application of this approach to a more realistic case, which is described in the following section.

4. Time-dependent WTD Model

We now present a time-dependent simulation of the solar corona obtained with the WTD model of Mikić et al. (2018), driven with the transverse electric field from Equations (4)–(5) and the radial electric field from method A. As input to the model, we used 720 1 hr cadence frames of the ESFAM model (Schrijver & DeRosa 2003), which corresponds to 30 days of evolution, or just longer than one CR. This is the same model that is implemented within the PFSS package in SolarSoft as the SFT module, which routinely assimilates a photospheric magnetogram to best describe the surface conditions at a given time.

For this case we use a special "fake-Sun" ESFAM run designed to represent the typical conditions during solar minimum, including large-scale surface flows, the emergence and decay of bipolar patches, and the evolution of random flux across a range of scales. For our purposes, this type of

simulation is ideal because we can sidestep some of the typical systematics of SFT maps that assimilate data. These include (1) zero-point offsets for the entire map, because at a given assimilation step only a portion of an active region is observed, (2) unphysical evolution driven by the sweep of the assimilation window, introducing new data instantaneously, as it moves across the Sun at the solar rotation rate. We now describe these maps in more detail.

The main methodology for the formation of the SFT maps is described in Appendix A of Schrijver (2001), but we briefly summarize it here. The emergence pattern for bipoles is based on an automated process that randomly selects bipoles with values for their flux, location, and axial tilt based on power-law distributions derived from long-term observational statistics. Once the flux has emerged—a process that is scaled to the total flux of the bipole—the polarities advect and cancel with nearby flux independently of each other. For very large bipoles (i.e., active regions), the flux is emerged as a group of smaller bipoles that aggregate to the characteristics listed above. Smaller bipoles with similarly randomized qualities (and a correspondingly larger latitudinal distribution) are also emerged in order to create a realistic background and distribution of the total flux. To process this total flux and model the cancellation on the correct timescales, there is an additional exponential flux removal term (described in Schrijver et al. 2002).

The flux in the SFT module was advected with the differential rotation profile taken from Table 1 of Komm et al. (1993a), in the case of the 1D cross-correlation analysis applied to Kitt Peak magnetogram data from 1975 to 1991:

$$\Omega(\lambda) = A + B\sin^2(\lambda) + C\sin^4(\lambda). \tag{24}$$

The above is a general functional form for differential rotation fits. Here Ω means the sidereal rotation rate, and λ is latitude. The coefficients measured by Komm et al. (1993a) are

$$A = 14.42 \text{ deg day}^{-1}$$

 $B = -2.00 \text{ deg day}^{-1}$
 $C = -2.09 \text{ deg day}^{-1}$. (25)

As implemented in the SFT model, a Carrington frame of reference is used, and so the solid-body sidereal CR rate of 14.18 deg day⁻¹ is subtracted off from A. In addition, in the SFT model, the rotation profile does not change with time (i.e., no torsional oscillations are present, etc.).

The meridional flow profile M is slightly more ad hoc but still takes its cues from empirical measurements. Like the differential rotation profile, it is implemented in the SFT model data as a constant-in-time function and does not vary.

The SFT model's profile was originally based on the measurements described in Komm et al. (1993b), which are of the form $M = f[\sin(2\theta)]$, or more specifically, $\sin(2\theta)$ is the leading term in an expression also involving $\sin(4\theta)$. However, the current SFT model ignores those fourth-order terms and also includes a tapering function applied to the polar latitudes, so that the functional form looks as follows:

$$M(\theta) = v_{A} \sin(2\theta) g(\theta) g(\pi - \theta). \tag{26}$$

Here M is the meridional flow speed, and θ is colatitude, with the coefficient v_A set to 12.7 m s⁻¹. Note that we

could switch from latitude to colatitude since $\sin(2 \operatorname{lat.}) = \sin(2 \operatorname{colat.})$. The tapering functions g only apply poleward of 40° in each hemisphere:

$$g(\theta) = 1 - \exp(-a\theta^3)$$

$$g(\pi - \theta) = 1 - \exp(-a[\pi - \theta]^3),$$
 (27)

where a=3.0. Without these tapering functions, the meridional flow will concentrate flux too close to the poles in the SFT model, in contrast to observations in which it is evident that the polar cap flux during solar minimum intervals is more spread out. Schrijver & Title (2001) felt justified in using this tapering function given the higher uncertainties of measurements of meridional flows near the poles. Note that this meridional flow profile is functionally similar to that given in Equation (3) of Schrijver & Title (2001) but with different values of v_A and a (these values can be found in Barnes et al. 2023).

4.2. Properties of the Simulation

The ESFAM/SFT maps were given as input to the MHD WTD model (Mikić et al. 2018; Török et al. 2018). For the latter we used a nonuniform grid in $r \times \theta \times \phi$ of $269 \times 181 \times 361$ points extending from 1 to 30 R_{\odot} . The smallest radial grid spacing at r = 1 R_{\odot} was ~ 400 km, the angular resolution in θ ranged between 0.8 at the equator and 1.7 at the poles, and the ϕ mesh was uniform. To dissipate structures that cannot be resolved since they are smaller than the cell size, we prescribed a uniform resistivity η corresponding to a resistive diffusion time $\tau_R \sim 4 \times 10^2$ hr, which is much lower than the value in the solar corona. The Alfvén travel time at the base of the corona ($\tau_{\rm A} = R_{\odot}/V_{\rm A}$) for $|\boldsymbol{B}| = 2.205 \,\mathrm{G}$ and $n_0 = 10^8 \,\mathrm{cm}^{-3}$, which are typical reference values, is 24 minutes (Alfvén speed $V_A = 480 \, \mathrm{km \, s^{-1}}$), so the Lundquist number τ_R/τ_A was 1×10^5 . In addition, in order to dissipate unresolved scales without substantially affecting the global solution, we introduced a uniform viscosity ν , corresponding to a viscous diffusion time τ_{ν} such that $\tau_{\rm A}/\tau_{\nu} = 0.015$. We prescribed fixed chromospheric values of density and temperature at the base of the domain of $n_0 = 4 \times 10^{12} \,\mathrm{cm}^{-3}$ and $T_0 = 17,500 \,\mathrm{K}$, respectively. These values were set to form a chromospheric "temperature plateau" that remains sufficiently large (Lionello et al. 2009) during the calculation no matter how large the heating.

For the coronal heating term, we use the same WTD model parameters as the simulation described in Boe et al. (2021, 2022), which is a slight update to the numbers used in Mikić et al. (2018). The Poynting flux of wave energy is prescribed at the base of the corona through an amplitude of the Elsässer variable $z_0 = 9.63 \,\mathrm{km \, s^{-1}}$, and we set the transverse correlation scale $\lambda_0 = 0.02 R_\odot$ along with a scaling factor $B_0 = 8.53 \,\mathrm{G}$ such that $\lambda_\perp = \lambda_0 \,\sqrt{B_0/B}$ in the corona. Similar to Mikić et al. (2018), we add two small exponential heating terms to heat the low corona: $H_0 = 2.7 \times 10^{-5} \,\mathrm{erg \, cm^{-3} \, s^{-1}}$, $\lambda_0 = 0.03 R_\odot$; $H_0 = 1.6 \times 10^{-8} \,\mathrm{erg \, cm^{-3} \, s^{-1}}$, $\lambda_0 = R_\odot$. Likewise, the wave pressure was specified from the Wentzel-Kramers–Brillouin model (Lionello et al. 2009).

We started the calculation using the first of the 720 magnetic flux maps to calculate a potential field extrapolation. The plasma temperature, density, and velocity were imposed from a 1D solar wind solution that had been calculated previously. Then, we advanced the MHD equations for about 80 hr to relax the system to a steady state. After the relaxation was

accomplished, we turned the surface evolution on. The differential rotation and meridional flow parameters were the same as those of Equation (25), except that, since our model is in the corotating frame of reference of the Sun, $A = 0.24 \, \text{deg day}^{-1}$ for us

We apply method A to Equations (4)–(5), using A = 1/4 for Equation (16) and D = 10 for Equation (20), to drive the MHD model for a CR.

4.3. Coronal Evolution

The left panel of Figure 3 and its associated online animation show the B_r field evolution during the course of the simulation, while the right panel shows the open field for the same times. The evolution of B_r at higher latitudes is dominated by differential rotation, and it is possible for the eye to pick up features as they are advected from west (right) to east (left), particularly in the associated animation available online. A few of the most prominent of these dynamic regions are indicated with circles in the figure. The black (left) and gold (right) rectangles appearing in all panels in the figure highlight a particularly persistent and complex region of mostly open field with a sizable embedded parasitic polarity; the whole feature drifts slowly to solar east over time owing to differential rotation, and the open field in the area changes significantly during the month of simulated time.

However, at lower latitudes, differential rotation becomes less and less discernible, while emergence and dispersion of magnetic flux become dominant. The magenta circle in the same panels shows a relatively strong bipolar region that is present at the beginning of the simulation and that undergoes decay and dissipation. Other rectangles and circles denote open-field and flux emergence regions, respectively, that are more dynamic or that emerge during the course of the simulation.

The results of these time-dependent effects on simulated emission are illustrated in Figures 4 and 5. We use the temperature and density from the simulation to forward-model the emission in the SDO AIA 171 Å channel for this figure. The left column of Figure 4 shows a 3D projection observed from an Earth-like point of view at the same times as the preceding figures (i.e., the longitude of the observer changes with the CR rate). To better understand the evolution of the emission, we can compute Carrington latitude—longitude maps of forward-modeled AIA emission by integrating along the radial direction for all points on the model. These are shown in the right column of Figure 4, with the same annotations as the preceding figure to aid in by-eye comparisons. Here the bipoles appear as bright active regions, while particularly bright patches within the active regions that evolve rapidly (best seen in the associated animation) are signatures of thermal nonequilibrium within these areas of highly stratified heating. The open fields contain somewhat lower emission than the closed field, though not as dark as would be expected from a highertemperature emission line (such as 193 Å, shown in the following figure).

In Figure 5 we show the surface B_r prescribed at the lower boundary, overlaid with forward-modeled SDO AIA 193 Å emission. This composite presentation shows the close relationship between the changing magnetic boundary conditions and the coronal evolution. Features visible in emission in the polar coronal holes are matched by the unipolar signatures in the underlying B_r map and are likewise advected by

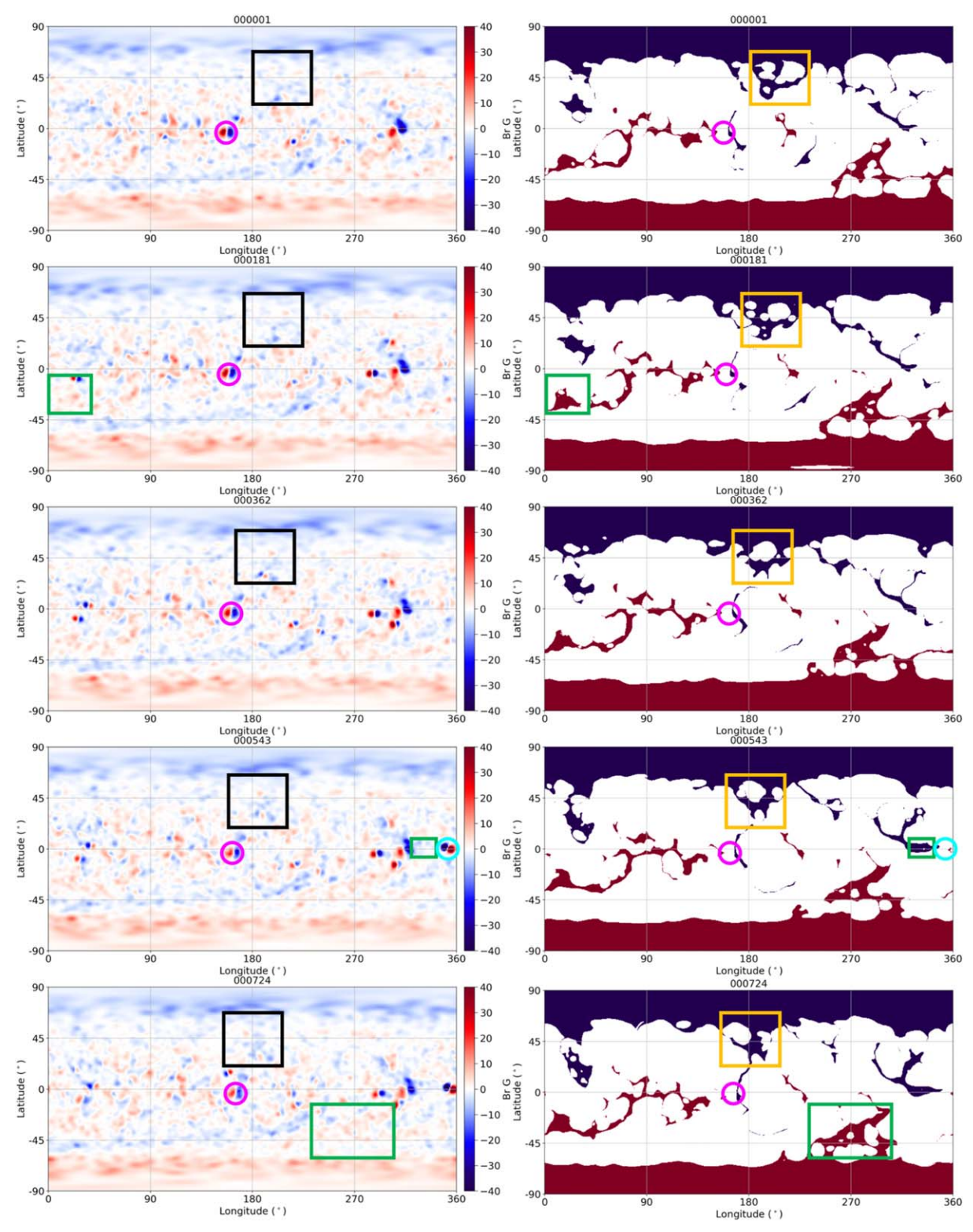


Figure 3. Evolution of the photospheric magnetic field and the open flux boundaries over 1 month in the time-evolving MHD model. The left panels show B_r , derived from the ESFAM flux transport model, as a latitude—longitude map. These are the boundary maps for the calculation. The right panels show open/closed boundaries (coronal holes) in the same format, with dark red indicating outward (positive) polarity, dark blue showing inward (negative) polarity, and white indicating closed-field regions. Five time instances are shown, from top to bottom: t = 0, $t \simeq 180$ hr, $t \simeq 360$ hr, $t \simeq 540$ hr, and $t \simeq 720$ hr. The box in every panel (black on the left, gold on the right for visibility) highlights a persistent open-field region, while the magenta circle near the center of each panel indicates a bipole that undergoes decay. Other rectangles and circles denote more transient open-field and flux emergence regions, respectively. A 7 s animation of this figure is available online (www.predsci.com/corona/tdc/animations/RL_2023_Fig3.mp4) showing both maps for the duration of the simulation time.

(An animation of this figure is available.)

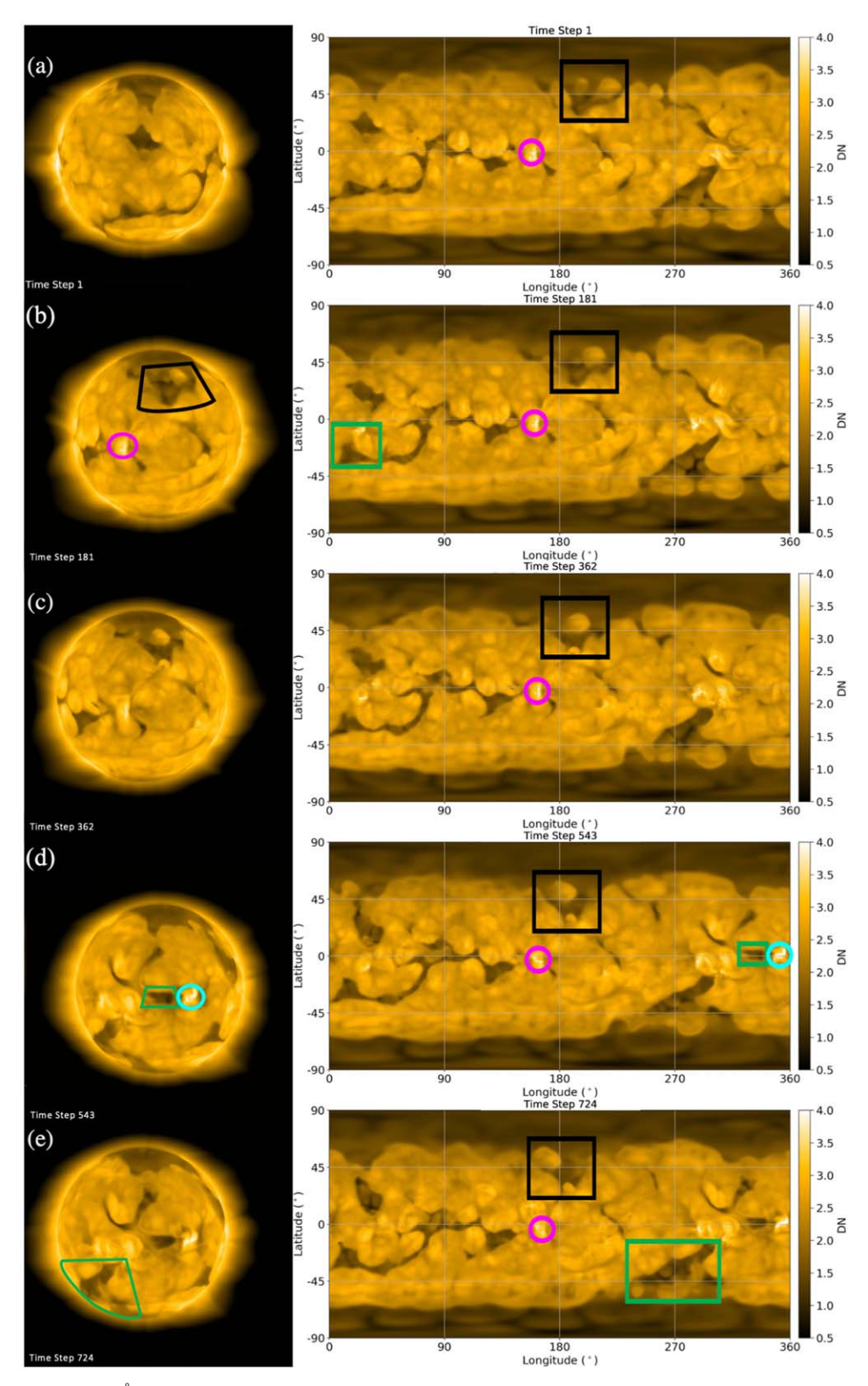


Figure 4. The emission in the AIA 171 Å channel over 1 month in the time-evolving MHD model. The left panels show the Sun from the point of view of an observer on Earth, as the star completes a full rotation around its axis. The right panels show a projection of the emission as a latitude—longitude map; the annotations are analogous to those from the previous figure. Five time instances are shown, corresponding to those of Figure 3: (a) t = 0; (b) $t \approx 180$ hr; (c) $t \approx 360$ hr; (d) $t \approx 540$ hr; (e) $t \approx 720$ hr. A 7 s animation of this figure is available online (www.predsci.com/corona/tdc/animations/RL_2023_Fig4.mp4), showing both visualization styles for the duration of the simulation time.

(An animation of this figure is available.)

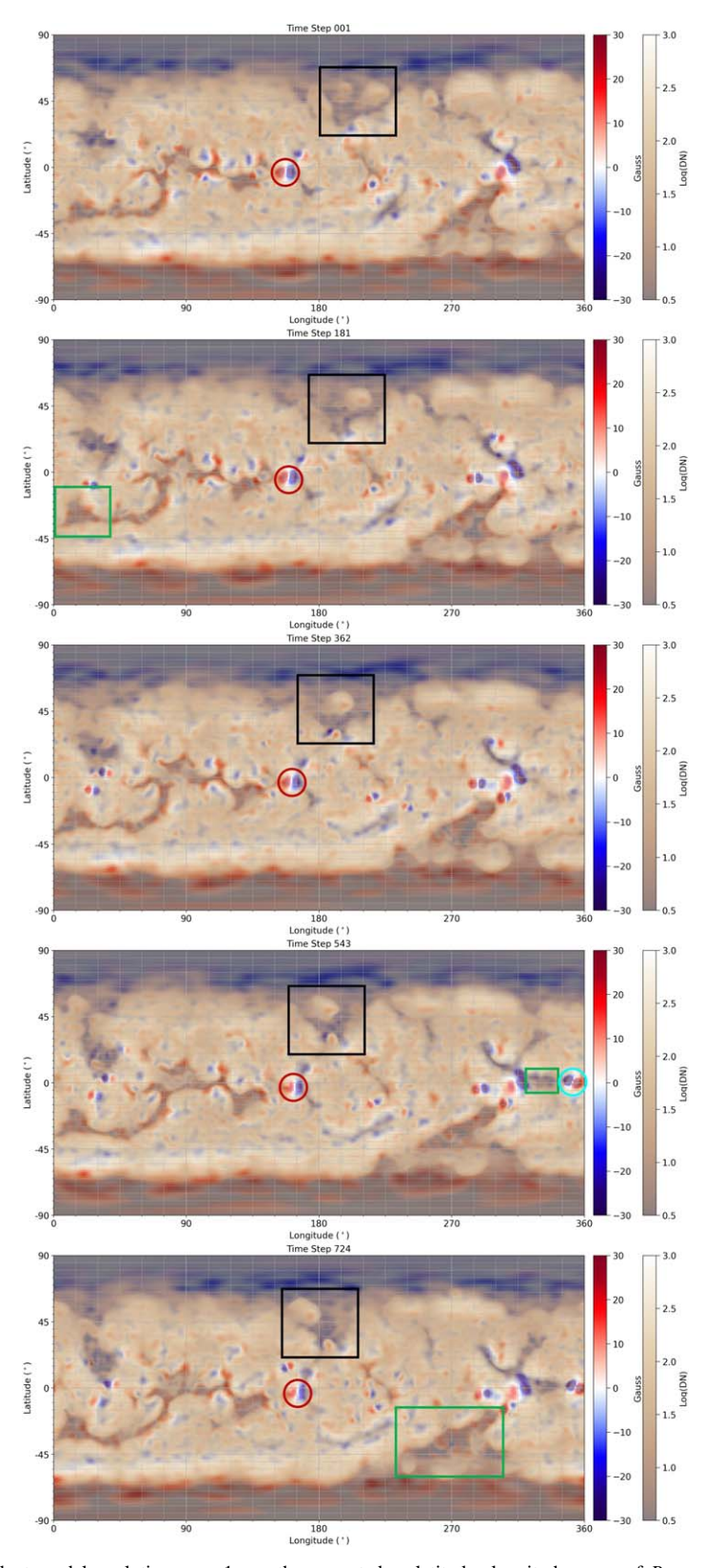


Figure 5. Time series of time-dependent model evolution over 1 month, presented as latitude—longitude maps of B_r overlaid with forward-modeled log-scaled synthetic SDO AIA 193 Å emission from the temperature and density of the model (Lionello et al. 2009). The black boxes indicate the same persistent open-field region throughout the simulation; green boxes illustrate several other open-field areas. The red circles indicate a persistent bipole, which decays during the simulation. The cyan circle shows a bipole that emerges during the course of the simulation. A 7 s animation of this figure is available online (www.predsci.com/corona/tdc/animations/RL_2023_Fig5.mp4), showing this map evolving over the full simulation time.

(An animation of this figure is available.)

differential rotation within the coronal holes. The black box repeated on each panel of Figure 5 highlights one such persistent open flux region. If only differential rotation were present, the open flux evolution would be (mostly) rigid, as observations (Timothy et al. 1975) show and as both potential (Wang et al. 1996) and MHD (Lionello et al. 2005) models indicate. However, magnetic flux evolution contributes to continuous changes in the boundary between the open- and closed-field regions. This is particularly evident in (but not limited to) the equatorial region between 270° and 360° longitude. Here on frame 543, flux emergence and open-field evolution are highlighted with the green box and cyan circle, respectively, which highlight an area in which emerging flux results in an expanded neighboring open-field region. In contrast, the red circle that appears in each panel illustrates a case of magnetic flux decay, as a bipolar region becomes more diffuse over the 1-month time frame of the simulation. Because of the richness of the EUV evolution and its relationship to interchange reconnection with open and closed fields, we explore the effects of these and related coronal signatures in the companion paper analyzing this simulation (Mason et al. 2023).

4.4. Dipped Field Lines

The Parker Solar Probe, during its first perihelion, discovered that the radial magnetic field was continuously interrupted by switchbacks on a timescale of less than a second to more than 1 hr (Dudok de Wit et al. 2020). Although our simulation was aimed at reproducing lower-frequency phenomena and at larger length scales, we also investigated the formation of dips in magnetic field lines. First, for each cell in the computational domain we determined whether there was a dip in its neighborhood by tracing a magnetic field segment and checking whether B_r changed sign along it. Then, from each point on an r = 19 R_{\odot} surface, we traced a field line and verified whether it passed through a cell having a dip. The resulting map is shown in Figure 6(a), where the seed points of dipped field lines are painted in white. Figure 6(b) has a map of s-logQ (signed logarithm of the squashing factor Q; Titov 2007) on the same surface. At low latitude, the so-called S-web generally coincides with the region where the slow solar wind is observed (Antiochos et al. 2011). A comparison between panels (a) and (b) indicates that dipped field lines have connections with the S-web. In particular, we enlarged two regions in the S-web map, the corresponding areas of the dipped field-line map, and superimposed them in panels (c) and (d). While the field lines associated with reversal in the sign of B_r lie along high-Q lines, only some have footpoints aligned with the current sheet (Figure 6(c)). Other dipped field lines cross single-polarity separatrices as in Figure 6(d). In panel (e), the dipped field-line map of panel (a) is shown as a semitransparent surface with two groups of representative field lines intersecting the areas of panels (c) and (d). Likewise, panel (f) presents the equivalent point of view for the s-logQmap. Panels (g) and (h) present 3D enlargements around the panel (c) and (d) areas, respectively. Some of the field lines in panel (g), which are all associated with the current sheet, are arranged in a flux rope. On the other hand, some of the field lines in panel (h), which are all associated with a same-polarity high-Q line, form a V shape, indicative of interchange reconnection (e.g., see Figures 5(c) and 6(c) of Lionello et al. 2005).

4.5. Charge States in the Static and Time-dependent Corona

To understand the effects of the continuous evolution of the surface magnetic fields on the ion charge-state distributions of the corona and solar wind, we compared the results of the timedependent model at $t = 524 \,\mathrm{hr}$ with its corresponding steadystate model. This steady-state corona (SSC) model was obtained by stopping all surface flows and magnetic flux evolution and letting the system relax for approximately 80 hr. We calculated the maxima of the C^{06}/C^{04} ratio along magnetic field lines. This is the ratio recommended by Landi & Lepri (2015) for analysis and comparison between models and in situ data because it is less sensitive to photoionization. In Figure 7 we show statistical distributions using either a linear (panel (a)) or a logarithmic (panel (b)) scale in the x-axis. The solid lines are associated with the SSC model, and the dotted lines are associated with the time-dependent corona (TDC) one. We distinguish four regions: loops (closed-field regions); coronal holes (open-field regions), which are mapped in panel (c); edge loops (i.e., long loops bordering open-field regions); and edge corona holes (i.e., open-field lines but close to closed-field areas), which appear in panel (d). Although the loop (violet) distributions are similar, we notice that the TDC model has a C^{06}/C^{04} distribution in coronal holes (green) that is significantly higher for smaller ratios than that of the SSC model. This is even more evident in the distribution of field lines at the edge of coronal holes (gold), with visibly higher distribution values for $C^{06}/C^{04} \lesssim 1$.

5. Discussion and Conclusion

We applied to our MHD model a technique that drives the evolution of the photospheric magnetic flux and of the surface flows to calculate the response of the solar corona. The electric field, which the technique provides, may be corrected with two methods to reduce the formation of current boundary layers. We tested the two corrective methods by comparing results with a simplified, reference simulation and found that either gives results in satisfactory agreement. We then used our technique with method A to calculate the evolution of the corona for a whole month, using a sequence of balanced magnetic flux maps obtained with the SFT module. From the simulation data, we produced emission images that show a continuous reconfiguration of the corona as active regions emerge and disperse and surface flows rearrange the flux. Dipped field lines that are formed during the computation appear to be associated with the S-web. In particular, we identified a flux rope in the current sheet, while field lines of single-polarity areas show the typical pattern of interchange reconnection. Ions' fractional charge states were evolved alongside the dynamics. The distributions of the C^{06}/C^{04} ion charge-state ratio appear to differ between the time-dependent model and the SSC. This difference is visible in the open-field regions, for which the time-dependent model has a distribution more skewed to lower charge states than the SSC, and particularly evident in the field lines close to the border of coronal holes.

Counterintuitively, it is the TDC model that has the lower ratios. The conventional wisdom for enhanced ratios in the slow wind is that they represent hotter plasma from closed loops that has been liberated through interchange reconnection. In the TDC model this can occur either by surface flows and/or evolution or by a thermal and/or tearing instability introducing

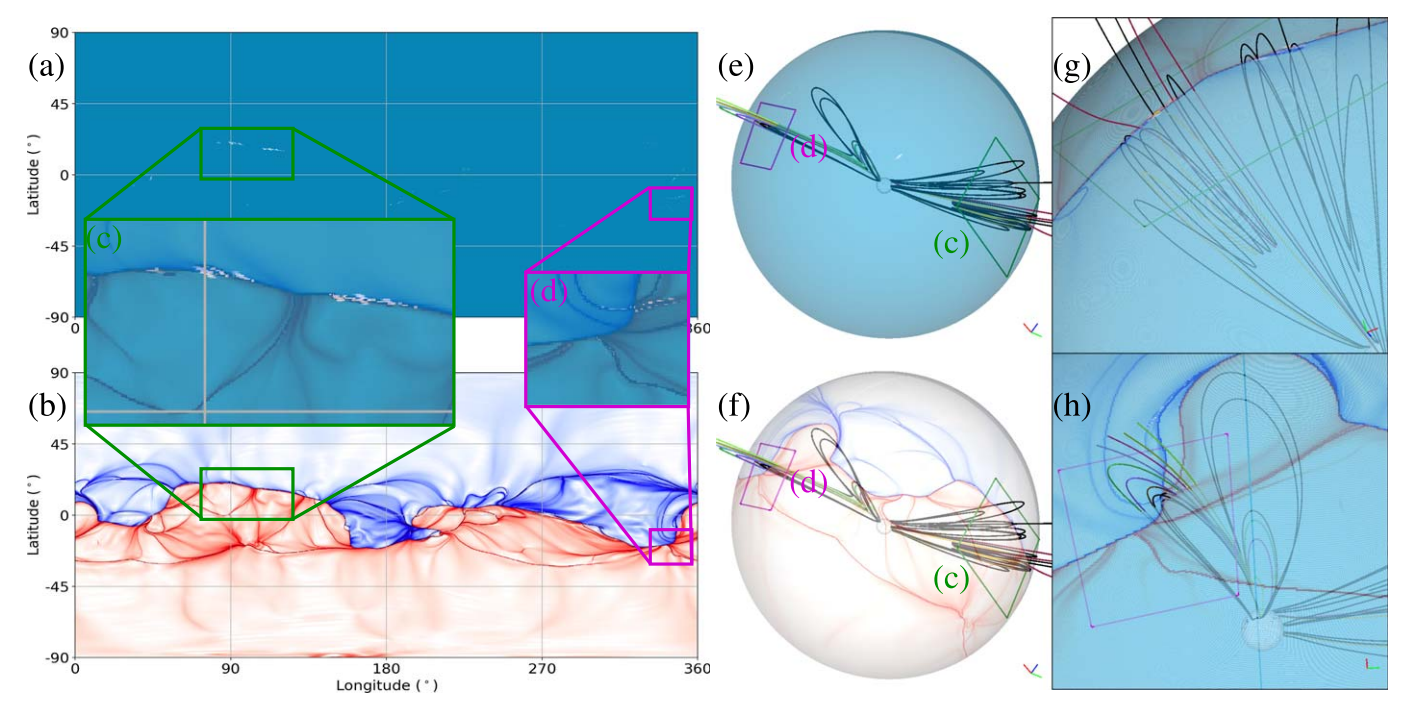


Figure 6. Dipped magnetic field lines (field lines that have a reversal of the sign of B_r) at t = 524 hr. (a) Footpoints of dipped field lines at r = 19 R_{\odot} as a latitude—longitude map. (b) Latitude—longitude map of $s-\log Q$ at the same height. (c) Enlargement and superposition of a region of panels (a) and (b) where the dipped field lines are associated with the current sheet. (d) Enlargement and superposition of another region of panels (a) and (b) where the dipped field lines are associated with a single-polarity separatrix line. (e) The r = 19 R_{\odot} semitransparent surface colored as in panel (a) with dipped field-line footpoints and marked with the panel (c) and (d) regions. Representative field lines are visible, and the solar surface is at the center. (f) The same as panel (e), but colored as in panel (b) with $s-\log Q$. (g) 3D enlargement of the panel (c) region with magnetic field lines. The solar surface is at the bottom right. (h) 3D enlargement of the panel (d) region with magnetic field lines.

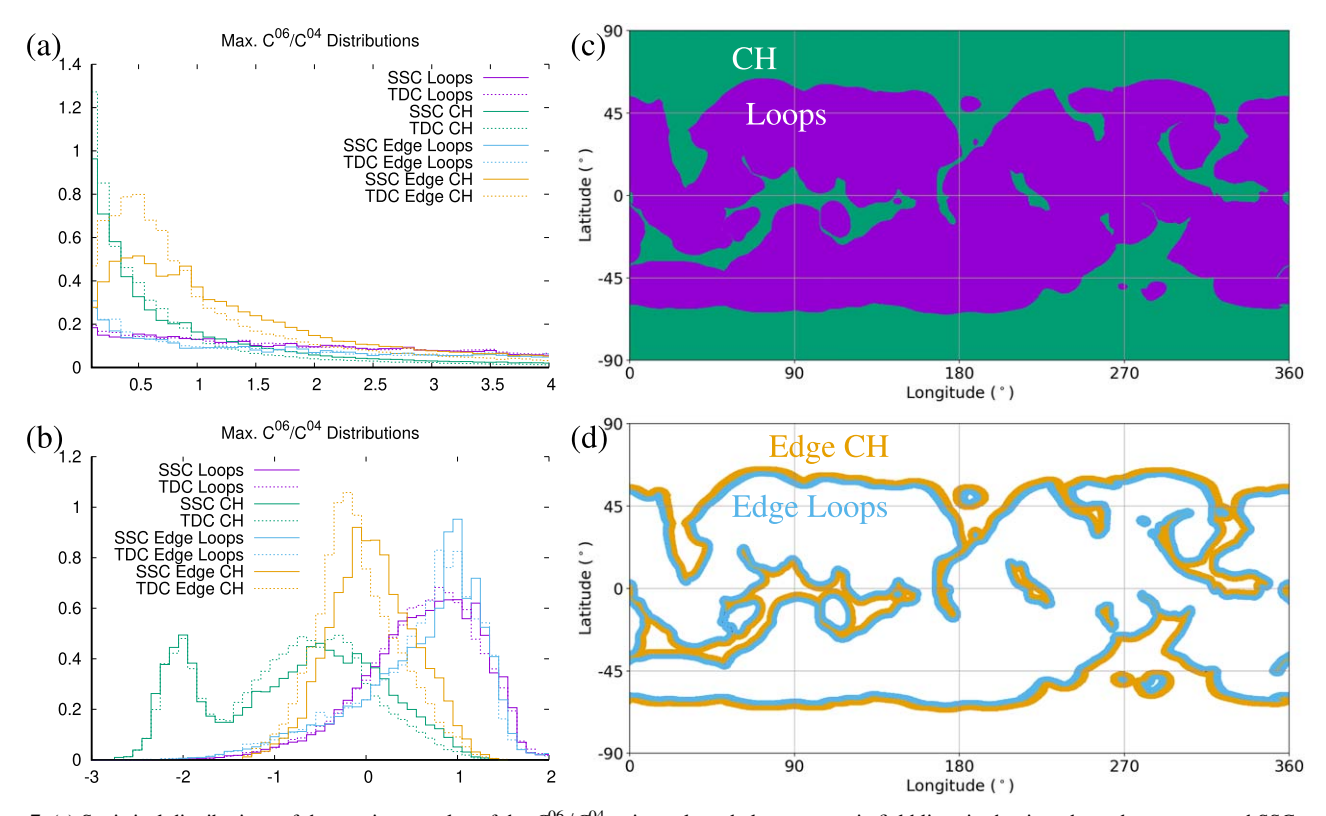


Figure 7. (a) Statistical distributions of the maximum value of the C^{06}/C^{04} ratio evaluated along magnetic field lines in the time-dependent corona and SSC models. We show distributions for loops (i.e., closed-field regions), coronal holes (open-field regions), loops at the edge of open-field areas, and edges of coronal holes. (b) The same as panel (a), but with a logarithmic scale for the axes. (c) The areas over which the loop (violet) and coronal hole (green) distributions are defined. (d) The same as panel (c), but for the edge loop (cyan) and edge coronal hole (gold) distributions.

reconnection at the streamer cusp itself (e.g., Réville et al. 2020), while in the SSC model this can only occur through the latter processes. On the other hand, the TDC model is slightly more open, and the streamer loops naturally have a shorter lifetime as the surface flux evolves and their geometry changes in time, leading to a lower temperature on average. It seems that in this case, with relatively modest resolution and minimal energization in the transverse field (Section 2.2), the latter process wins out. In future work we aim to study how additional shear (helicity) that emerges at global scales will influence the charge-state ratios, as well as the role of small-scale flux patches that induce interchange reconnection near the coronal base as they evolve (e.g., Sterling & Moore 2020; Bale et al. 2022).

Ultimately we have demonstrated a practical technique for time-dependently driving a global coronal model from only a sequence of magnetic maps. This leads to an inherent time evolution of features in the model corona that is not possible to capture with traditional steady-state methods. Such a capability is crucial for answering long-standing questions about how closed and open fields evolve in the corona and how the field and plasma properties of the observed slow solar wind are formed. Lastly, with the advent of modern SFT models that readily assimilate observations to produce time sequences of full-Sun magnetic maps, we expect simple but robust driving techniques like those introduced here to play a key role in the next generation of solar wind and CME models.

Acknowledgments

This work was supported by the NASA Heliophysics Living With a Star Science and Strategic Capabilities programs (grant Nos. 80NSSC20K0192, 80NSSC22K1021, and 80NSSC22K0893), the NASA Heliophysics System Observatory Connect program (grant No. 80NSSC20K1285), and the NSF PREEVENTS program (grant ICER1854790). Computing resources supporting this work were provided by the NASA High-End Computing (HEC) Program through the NASA Advanced Supercomputing (NAS) Division at Ames Research Center and by the Expanse supercomputer at the San Diego Supercomputing Center through the NSF ACCESS and XSEDE programs. M.L.D. acknowledges support from NASA under contract NNG04EA00C as part of the AIA science team.

ORCID iDs

Roberto Lionello https://orcid.org/0000-0001-9231-045X Cooper Downs https://orcid.org/0000-0003-1759-4354 Emily I. Mason https://orcid.org/0000-0002-8767-7182 Jon A. Linker https://orcid.org/0000-0003-1662-3328 Ronald M. Caplan https://orcid.org/0000-0002-2633-4290 Pete Riley https://orcid.org/0000-0002-1859-456X Viacheslav S. Titov https://orcid.org/0000-0001-7053-4081 Marc L. DeRosa https://orcid.org/0000-0002-6338-0691

References

Antiochos, S. K., Mikić, Z., Titov, V. S., Lionello, R., & Linker, J. A. 2011,

```
ApJ, 731, 112
Arge, C. N., Henney, C. J., Koller, J., et al. 2010, American Institute of Physics Conf. Ser., Twelfth International Solar Wind Conf., 1216 ed. M. Maksimovic et al. (New York: AIP), 343
Bale, S. D., Drake, J. F., McManus, M. D., et al. 2023, Natur, 618, 252
Barnes, G., DeRosa, M. L., Jones, S. I., et al. 2023, ApJ, 946, 105
```

Benz, A. O. 2017, LRSP, 14, 2

```
Boe, B., Habbal, S., Downs, C., & Druckmüller, M. 2021, ApJ, 912, 44
Boe, B., Habbal, S., Downs, C., & Druckmüller, M. 2022, ApJ, 935, 173
Breech, B., Matthaeus, W. H., Minnie, J., et al. 2008, JGRA, 113, 8105
Chandran, B. D. G., & Hollweg, J. V. 2009, ApJ, 707, 1659
Cheung, M. C. M., & DeRosa, M. L. 2012, ApJ, 757, 147
Cranmer, S. R., van Ballegooijen, A. A., & Edgar, R. J. 2007, ApJS, 171, 520
Dere, K. P., Landi, E., Mason, H. E., Monsignori Fossi, B. C., & Young, P. R.
   1997, A&AS, 125, 149
Dmitruk, P., Milano, L. J., & Matthaeus, W. H. 2001, ApJ, 548, 482
Downs, C., Linker, J. A., Mikić, Z., et al. 2013, Sci, 340, 1196
Dudok de Wit, T., Krasnoselskikh, V. V., Bale, S. D., et al. 2020, ApJS,
Fisher, G. H., Welsch, B. T., Abbett, W. P., & Bercik, D. J. 2010, ApJ,
   715, 242
Fisk, L. A., & Kasper, J. C. 2020, ApJL, 894, L4
Fritsch, F. N., & Carlson, R. E. 1980, SJNA, 17, 238
Heinemann, M., & Olbert, S. 1980, JGR, 85, 1311
Higginson, A. K., Antiochos, S. K., DeVore, C. R., Wyper, P. F., &
   Zurbuchen, T. H. 2017, ApJL, 840, L10
Jin, M., Manchester, W. B., van der Holst, B., et al. 2012, ApJ, 745, 6
Kepko, L., Viall, N. M., Antiochos, S. K., et al. 2016, GeoRL, 43, 4089
Komm, R. W., Howard, R. F., & Harvey, J. W. 1993a, SoPh, 145, 1
Komm, R. W., Howard, R. F., & Harvey, J. W. 1993b, SoPh, 147, 207
Landi, E., & Lepri, S. T. 2015, ApJL, 812, L28
Landi, E., Young, P. R., Dere, K. P., Del Zanna, G., & Mason, H. E. 2013,
   ApJ, 763, 86
Linker, J. A., Lionello, R., Mikić, Z., Titov, V. S., & Antiochos, S. K. 2011,
   ApJ, 731, 110
Linker, J. A., Mikić, Z., Biesecker, D. A., et al. 1999, JGR, 104, 9809
Linker, J. A., Mikić, Z., Lionello, R., et al. 2003, PhPl, 10, 1971
Lionello, R., Downs, C., Linker, J. A., et al. 2013, ApJ, 777, 76
Lionello, R., Downs, C., Linker, J. A., et al. 2019, SoPh, 294, 13
Lionello, R., Linker, J. A., & Mikić, Z. 2009, ApJ, 690, 902
Lionello, R., Linker, J. A., Mikić, Z., & Riley, P. 2006, ApJL, 642, L69
Lionello, R., Riley, P., Linker, J. A., & Mikić, Z. 2005, ApJ, 625, 463
Lionello, R., Titov, V. S., Mikić, Z., & Linker, J. A. 2020, ApJ, 891, 14
Luhmann, J. G., Li, Y., Lee, C. O., et al. 2022, SpWea, 20, e2022SW003110
Lumme, E., Pomoell, J., & Kilpua, E. K. J. 2017, SoPh, 292, 191
Mason, E. I., Lionello, R., Downs, C., Linker, J. A., & Caplan, R. M. 2023,
   ApJ, submitted, arXiv:2306.11956
Matthaeus, W. H., Zank, G. P., Oughton, S., Mullan, D. J., & Dmitruk, P.
   1999, ApJL, 523, L93
Mikić, Z., Downs, C., Linker, J. A., et al. 2018, NatAs, 2, 913
Mikić, Z., Linker, J. A., Schnack, D. D., Lionello, R., & Tarditi, A. 1999, PhPl,
Odstrcil, D., Mays, M. L., Hess, P., et al. 2020, ApJS, 246, 73
Oran, R., Landi, E., van der Holst, B., et al. 2015, ApJ, 806, 55
Raouafi, N. E., Patsourakos, S., Pariat, E., et al. 2016, SSRv, 201, 1
Réville, V., Velli, M., Rouillard, A. P., et al. 2020, ApJL, 895, L20
Riley, P., Linker, J. A., Mikić, Z., et al. 2006, ApJ, 653, 1510
Schnack, D. D., Barnes, D. C., Mikic, Z., Harned, D. S., & Caramana, E. J.
   1987, JCoPh, 70, 330
Schrijver, C. J. 2001, ApJ, 547, 475
Schrijver, C. J., & DeRosa, M. L. 2003, SoPh, 212, 165
Schrijver, C. J., De Rosa, M. L., & Title, A. M. 2002, ApJ, 577, 1006
Schrijver, C. J., & Title, A. M. 2001, ApJ, 551, 1099
Scott, R. B., Pontin, D. I., Antiochos, S. K., DeVore, C. R., & Wyper, P. F.
   2021, ApJ, 913, 64
Shen, C., Raymond, J. C., Murphy, N. A., & Lin, J. 2015, A&C, 12, 1
Sokolov, I. V., van der Holst, B., Oran, R., et al. 2013, ApJ, 764, 23
Solanki, S. K., del Toro Iniesta, J. C., Woch, J., et al. 2020, A&A, 642, A11
Sterling, A. C., & Moore, R. L. 2020, ApJL, 896, L18
Szente, J., Landi, E., & van der Holst, B. 2022, ApJ, 926, 35
Telloni, D., Zank, G. P., Stangalini, M., et al. 2022, ApJL, 936, L25
Timothy, A. F., Krieger, A. S., & Vaiana, G. S. 1975, SoPh, 42, 135
Titov, V. S. 2007, ApJ, 660, 863
Török, T., Downs, C., Linker, J. A., et al. 2018, ApJ, 856, 75
Upton, L., & Hathaway, D. H. 2014, ApJ, 780, 5
Usmanov, A. V., Matthaeus, W. H., Breech, B. A., & Goldstein, M. L. 2011,
   ApJ, 727, 84
van der Holst, B., Sokolov, I. V., Meng, X., et al. 2014, ApJ, 782, 81
Velli, M. 1993, A&A, 270, 304
Verdini, A., & Velli, M. 2007, ApJ, 662, 669
Wang, Y.-M., Hawley, S. H., & Sheeley, N. R. 1996, Sci, 271, 464
Wang, Y. M., Sheeley, N. R. J., & Nash, A. G. 1991, ApJ, 383, 431
```

Webb, D. F., & Howard, T. A. 2012, LRSP, 9, 83

```
Weinzierl, M., Yeates, A. R., Mackay, D. H., Henney, C. J., & Arge, C. N.
  2016, ApJ, 823, 55
```

Worden, J., & Harvey, J. 2000, SoPh, 195, 247

Wyper, P. F., Antiochos, S. K., DeVore, C. R., et al. 2021, ApJ, 909, 54 Yeates, A. R. 2017, ApJ, 836, 131

Yeates, A. R., Amari, T., Contopoulos, I., et al. 2018, SSRv, 214, 99

Zank, G. P., Jetha, N., Hu, Q., & Hunana, P. 2012, ApJ, 756, 21 Zank, G. P., Matthaeus, W. H., & Smith, C. W. 1996, JGR, 101, 17093 Zank, G. P., Nakanotani, M., Zhao, L. L., Adhikari, L., & Kasper, J. 2020, ApJ,

Zurbuchen, T. H., Fisk, L. A., Gloeckler, G., & von Steiger, R. 2002, GeoRL, 29, 66